ACS APPLIED MATERIALS & INTERFACES

www.acsami.org Research Article

Wearable Circuits Sintered at Room Temperature Directly on the Skin Surface for Health Monitoring

Ling Zhang, Hongjun Ji, Houbing Huang, Ning Yi, Xiaoming Shi, Senpei Xie, Yaoyin Li, Ziheng Ye, Pengdong Feng, Tiesong Lin, Xiangli Liu, Xuesong Leng, Mingyu Li, Jiaheng Zhang, Xing Ma, Peng He,* Weiwei Zhao,* and Huanyu Cheng*

Cite This: https://dx.doi.org/10.1021/acsami.0c11479 Read Online

ACCESS | Metrics & More | Article Recommendations | Supporting Information

ABSTRACT: A soft body area sensor network presents a promising direction in wearable devices to integrate on-body sensors for physiological signal monitoring and flexible printed circuit boards (FPCBs) for signal conditioning/readout and wireless transmission. However, its realization currently relies on various sophisticated fabrication approaches such as lithography or direct printing on a carrier substrate before attaching to the body. Here, we report a universal fabrication scheme to enable printing and room-temperature sintering of the metal nanoparticle on paper/fabric for FPCBs and directly on the human skin for on-body sensors with a novel sintering aid layer. Consisting of polyvinyl alcohol (PVA) paste and nanoadditives in the water, the sintering aid layer reduces the sintering temperature. Together with the significantly decreased surface roughness, it allows for the integration of a submicron-thick conductive pattern with enhanced electromechanical performance. Various on-body sensors integrated with an FPCB to detect health conditions illustrate a system-level example.

KEYWORDS: *body area sensor network, flexible printed circuit boards, directly printed on-body sensors, room-temperature sintering, sintering aid layer*

1. INTRODUCTION

Skin-interfaced, wearable electronics have attracted significant attention because of their unique role from preventative monitoring and diagnostic confirmation to convenient therapeutic options.[1,2] The ultimate application of these biointegrated devices for practical and convenient applications hinges on the seamless integration of on-body sensors with wireless transmission modules. Multifunctional on-body sensors can precisely and continuously monitor the health conditions of the human body, whereas the wireless transmission modules can wirelessly power up the sensors and transmit the data generated from them to the cloud for the healthcare professionals. As a promising direction toward this class of integrated systems, the soft body area sensor network includes on-body sensors for physiological signal monitoring and flexible printed circuit boards (FPCBs) for signal conditioning/readout and wireless transmission. In contrast to the conventional PCBs, the paper/textile-based FPCBs are essential for the wearable electronics because of their flexible and biocompatible properties.[3−5] Although the textile-based FPCBs can be directly integrated into clothing, the low-cost paper-based FPCBs also allow temporary use and easy replacement on different clothing locations.[6,7] Compared with other wearable devices, the on-body sensors that pliably laminate on the skin surface can precisely capture the clinically relevant data for health monitoring.[8,9] Realization of the soft body area sensor network currently relies on various sophisticated fabrication approaches from lithography and transfer printing[10,11] to direct printing,[12,13] especially when stretchable sensors are separated from readout circuits (e.g., FPCBs).[14,15] In particular, extensive efforts have been devoted for exploring the integration of wearable electronics on paper/fabric[14,16,17] or human skin.[18,19] However, there lacks a simple yet universal approach to fabricate all of the modules relevant to the soft body area sensor network because of the challenging requirements of low-temperature processing on textured surfaces with easy removal capabilities. Although many existing studies have demonstrated the room temperature processing of Ag nanoparticle (NP) ink with laser, high pressure, microwave, or chemical treatment,[20−23] they cannot be used to directly fabricate sensors on the human skin. By considering the expensive equipment, complicated procedures, and increasing

Received: June 24, 2020
Accepted: September 11, 2020
Published: September 11, 2020

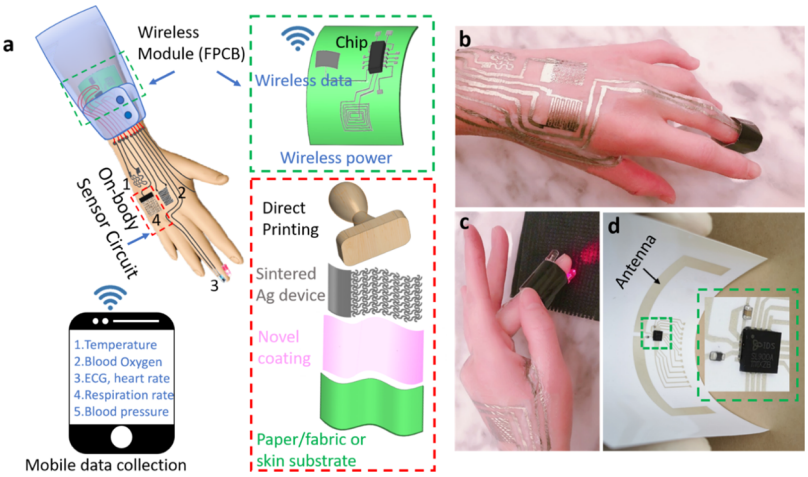

Figure 1. Schematic and proof-of-the-concept demonstration of a soft body area sensor network consisting of various on-body sensors and a FPCB. (a) Design concept of the soft body area sensor network. The paper/fabric-based FPCB on clothing can integrate wireless data and power transmission modules (e.g., bluetooth or near-field communication module), along with COTS chips for extended collection and processing of data (green box). The red box illustrates the simple process of preparing the directly printed on-body sensors sintered at room temperature. (b) Optical image of a hand with multiple on-body sensors (e.g., electrodes and temperature/hydration sensors) directly printed and sintered on the skin surface. (c) Optical image of a blood oxygen saturation measurement unit consisting of one red and one infrared LED and a photodiode on the fingertip. (d) Optical image of the paper-based FPCB that includes the SL900A UHF RFID sensing IC chip and the antenna.

electronic wastes from the existing fabrication approaches, it is even more pressing to develop a new fabrication technique to address all of these challenges.

In this article, we report a simple yet universally applicable fabrication technique with the use of a novel sintering aid layer to enable direct printing and room-temperature sintering of various metal inks for constructing paper/fabric-based FPCBs and on-body sensors. Consisting of the polyvinyl alcohol (PVA) paste and functional nanoadditives (e.g., TiO_2 or $CaCO_3$, among others), the sintering aid layer reduces the surface roughness of various substrates to allow printing of an ultrathin layer of metal patterns with improved electromechanical performance against bending and folding. More importantly, the metal NPs printed on the sintering aid layer have significantly decreased sintering temperature to form an FPCB on paper/textile or on-body sensors directly on the skin surface. Various on-body sensors integrated with an FPCB illustrate a system-level example of this technology.

2. INTEGRATED WEARABLE SYSTEM WITH VARIOUS ON-BODY SENSORS AND FPCBS

The schematic in Figure 1a presents an overview of the directly printed, room temperature-sintered, and hybrid skin-interfaced electronic devices, illustrating the design and working principle of the proposed system. The electronic system consists of sensors for vital signal measurements, commercial off-the-shelf (COTS) chips for extended data collection and processing, wireless data and power transmission modules, and paper/fabric-based FPCBs for system integration. The proof-of-concept demonstration includes representative sensors to measure temperature, hydration, electrocardiogram (ECG), electromyography (EMG), and blood oxygen saturation. As accurate assessment of human health conditions requires pliable sensor integration on the skin surface, the sensors directly printed on various positions of the human body establish the capability toward the envisioned functional operations (Figure 1b). Although the integration of various sensors (e.g., temperature, humidity, ECG, and EMG) can be easily achieved on a relative flat skin surface, the blood oxygen saturation measurement relies on the use of light-emitting diodes (LEDs) and a photodiode on a 3D curvilinear surface such as the fingertip (Figure 1c). Further miniaturization of the system is possible with the use of microscale LEDs (μ-LEDs).[24] A proof-of-concept demonstration of one paper-based FPCB consists of the SL900A UHF RFID sensing IC chip (SL900A-DK-STQFN 16, AMS, Austria), the antenna, and conductive traces with contact pads to connect the chip and various sensors (Figure 1d). Because the SL900A RF chip can be used to capture the resistive and capacitive sensing signals (Figure S1), this paper-based FPCB can be directly used for the wireless readout from the temperature and hydration sensors presented in this work. Both the direct sensor fabrication on the skin and preparation of the paper/fabric-based FPCBs are building on a sintering aid layer that enables low-temperature or even room-temperature sintering of directly printed metallic patterns (e.g., Ag). The sintering aid layer composed of nanoadditives (e.g., TiO_2 and $CaCO_3$) in the PVA paste not only reduces the sintering temperature of the metal NP inks printed on top but also improves the mechanical property of the substrate and electromechanical performance of the resulting electronic devices.

2.1. Design and Fabrication of Paper/Fabric-Based FPCBs. In contrast to the sensors conformal to the skin for accurate measurements, the paper- or fabric-based FPCBs can be placed nearby and connected to the sensors for data collection, processing, and transmission. As an alternative to the wires between the sensors and FPCBs, a body area sensor network (bodyNET) can be exploited to wirelessly link on-body sensor tags to readout circuits on the FPCBs.[25] Because of their affordable (~0.01 $/m^2) and lightweight properties, the paper is first selected and demonstrated as the substrate for fabricating the FPCBs. Although electronic circuits have previously been printed onto the paper substrate,[26−28] the electrical resistivity of the metal pattern on the paper substrate substantially increases as the surface roughness of the substrate increases because of the increased length in the conductive pathway.[29]

https://dx.doi.org/10.1021/acsami.0c11479
ACS Appl. Mater. Interfaces XXXX, XXX, XXX−XXX

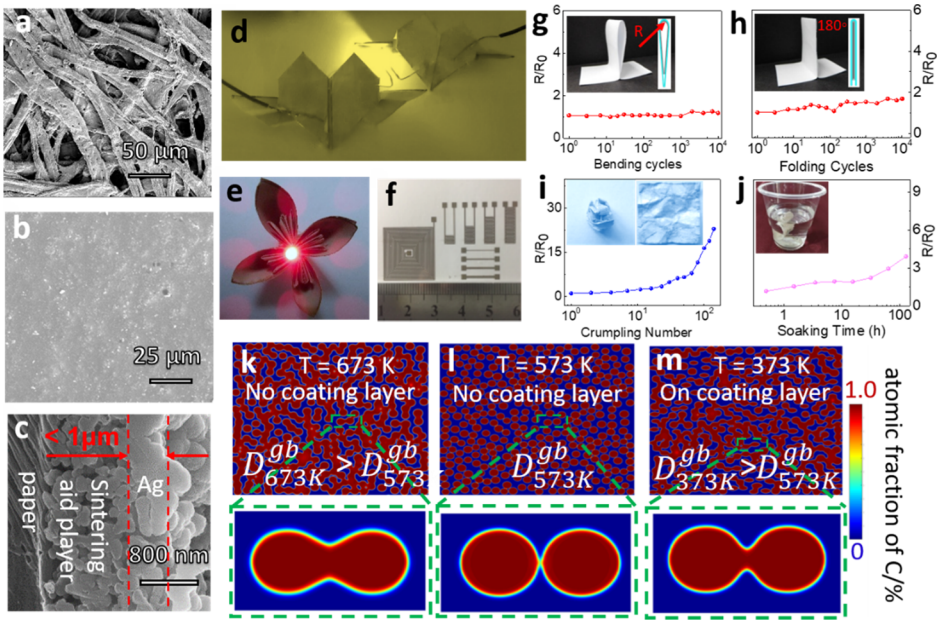

Figure 2. Performance demonstration of the paper/fabric-based FPCBs. SEM images of the copy paper (a) before and (b) after applying the sintering aid layer consisting of PVA paste and the TiO_2 nanoadditive and (c) its cross-sectional area of the interface with the sintering aid layer sandwiched between the copy paper and the sintered Ag NPs. Optical images of 3D origami paper structures folded into (d) heart and (e) flower shapes with the conductive Ag pattern intact to light up LEDs and (f) various printed patterns on the copy paper. Electromechanical performance of printed patterns against (g) bending for 10^4 times at a radius of R = 0.5 mm, (h) folding of the same sample for 10^4 times for origami/kirigami applications, and (i) crumpling and unfolding for 140 times. (j) Printing the conductive Ag pattern on a fabric substrate further demonstrates a stable conductive property after soaking in water for up to 100 h. Phase-field simulations of the sintering process between Ag NPs without the sintering aid layer at sintering temperatures of (k) 673 and (l) 573 K or (m) with the sintering aid layer at 373 K.

Prepared by dewatering a dilute suspension of natural cellulose fibers, the paper with a hierarchically porous structure surface (Figure 2a) presents challenges for direct ink printing during the fabrication of the FPCBs. Although the sintering aid layer can be coated on both hydrophobic and hydrophilic surfaces, the hydrophilic surface such as the paper (Figure S2) would enable a more uniform sintering aid layer. Coating the paper with a mixture of the PVA paste and TiO_2 nanoadditives significantly reduces its surface roughness (Figure 2b). The root mean square roughness measured by atomic force microscopy (AFM) decreases from 1573 to 412 nm after coating (Figure S3). The significantly reduced surface roughness allows for easy subsequent printing of Ag NP inks, followed by sintering at 120 °C. This observation is consistent with the previous literature report,[30] which also concludes the reduced sintering temperature of Ag NPs on the high-temperature-resistant paper with TiO_2 as the main component (Figure S4). As indicated by the scanning electron microscopy (SEM) image of the cross-sectional area, the sintering of Ag NPs occurs on the sintering aid layer with a thickness of ca. 1 μm (Figure 2c). It is interesting to note the Ag NPs away from the sintering aid layer remain unsintered, whereas those close to the sintering aid layer clearly show sintering necks. The solid-state sintering of Ag NPs with enhanced strength and electrical/thermal conductivities is likely attributed to the increased grain boundary diffusion of NPs, which will be explained in detail in the subsequent discussion. Nevertheless, removing the unsintered Ag NPs away from the sintering aid layer yields the designed conductive pattern with a much-reduced thickness (i.e., <1 μm in Figure 2c). The significantly reduced thickness further improves the mechanical property of the resulting patterns to ensure their robust property against bending because the bending stiffness or resistance scales with the cubic of the structure thickness. The remarkably stable electromechanical performance of the conductive pattern on paper enables the demonstration of various 3D origami or kirigami circuits, with LEDs brightly lit during shape transformation (Figure 2d,e). The electromechanical property of various printed patterns on paper (Figure 2f) has been characterized against bending with a radius of curvature of 0.5 mm (Figure 2g) and folding in origami/kirigami applications each for 10,000 cycles based on the same sample that has been bent (Figure 2h). The conductivity of various patterns based on sintered Ag NP ink on a paper with a size of 20 × 20 mm^2 also remains relatively stable as the paper is arbitrarily crumpled and unfolded for over 100 times (Figure 2i). The electrical and electromechanical properties of the sintered Ag pattern from this work compare favorably with those reported in the literature (Figure S5): metal NP ink with a diameter of less than 10 nm[17,31,32] and with nanoadditives in the ink.[33] Although many other studies have demonstrated the room temperature processing of Ag NP ink with laser, high pressure, microwave, or chemical treatments,[20−23] they cannot be used to directly fabricate sensors on the human skin. The versatility of the proposed approach is demonstrated using inks with different metal particles on various papers (e.g., printing, copy, and weighting papers) or porous substrates such as the fabric (e.g., cotton, chemical fabric, and silk) (Figure S6). The sintering aid layer is effective to reduce the surface roughness of all six substrate materials (Figure S7). In the proof-of-concept demonstration, six types of metal micro/nanoparticles (MPs/NPs) have been explored, including Ag NPs of ∼50 nm, Ag MPs of ∼2 or ∼40 μm, Ni NPs of ∼100 nm, Cu MPs of ∼1 μm, and Ni/Ag core/shell NPs of ∼50 nm. Although metal MPs/NPs with increasing sizes involve higher sintering temperatures because of lower surface activity, all six metal

https://dx.doi.org/10.1021/acsami.0c11479
ACS Appl. Mater. Interfaces XXXX, XXX, XXX−XXX

MPs/NPs selected in the demonstration can form conductive patterns with sintering temperatures lower than 120 °C (Figure S8). Owing to the small thickness of the sintered pattern and robust adhesion to the substrate, printed patterns based on these different metal particle inks on copy/printing/weighting paper substrates also exhibit excellent electromechanical performance (Figure S9). Compared to the cotton substrate, the patterns based on Ag NPs of ~50 nm on the chemical fabric or silk substrate only show small changes in the normalized resistance change upon bending with a radius of curvature of 0.5 mm for 10^5 times (Figure S10a). Owing to the excellent washability of the fabric, the conductive Ag pattern on the fabric substrate remains functional and relatively stable even after soaking in water for up to 100 h (Figures 2j and S10b). The performance of the fabric-based Ag pattern in solutions with different pH values from 4 to 9 and with a step size of 1 is further investigated. Although the relative resistance rapidly increases with the soaking time in the solution with a pH value of 8 or 9, the conductive Ag patterns on the fabric substrate are more stable in the acid solution (Figure S10c), with a pH value more relevant to sweat.[34] Further improvement could include the use of encapsulation layers as those commonly explored for transient materials.[35,36] The excellent electromechanical performance of the demonstrated FPCBs on paper or fabric highlights their potential for integration with various sensing modules on the clothing or skin that may undergo complex natural motions (e.g., bending, twisting, or wrinkling). Additionally, the robust performance against water or high moisture levels also ensures their application in biointegrated electronics during sweating conditions.

System investigation of the proposed approach based on a sintering aid layer and subsequent ink printing involves the use of various nanoadditives in the PVA paste at different concentration ratios (Tables S1 and 2). The electromechanical performance of the conductive pattern on the substrate with a sintering aid layer is improved as the ratio of PVA powder to water increases from 1:9 to 1:4, the ratio of TiO_2 to PVA paste decreases from 1:5 to 1:20, or the annealing temperature reduces from 160 to 120 °C (Figure S11). The reduced sintering temperature of Ag NPs with the use of the sintering aid layer can be attributed to the increased grain boundary diffusion coefficient (D^{gb})[37] from charge neutralization[38−40] than that with charged ions. It is apparent that anions (e.g., SO_3^{2-}, COO^-, and PO_3^{3-}) exist in the Ag NP ink to cause the Ag NPs negatively charged. Although there are no intrinsic cationic groups in the sintering aid layer with the TiO_2 nanoadditive and PVA paste, cationic radicals can form from the interaction between TiO_2 and PVA (Figure S12). As organic compounds with conjugated chains, the PVA has π-electrons in the conjugated p orbital of a double bond (C═C or C═O)[41] as a charge carrier to result in charge mobility along the chain of the polymer backbone.[42] In the PVA/TiO_2 system, the active −OH group on the surface of TiO_2 at relatively low temperature (100−200 °C) reacts with the −OH groups in PVA molecular chains to form C−O−Ti bonds through a dehydration reaction. The formed C−O−Ti bonds can act as the pathway to quickly transfer the excited electrons from PVA to TiO_2, resulting in cationic radical PVA* for charge neutralization.[39] The important role of the cationic radical can be confirmed in the experiment with the radical inhibitor (L-ascorbic acid) (Figure S13). After coating the sintering aid layer with L-ascorbic acid on the paper, the Ag NP ink printed and annealed at a temperature of 120 °C yields a nonconductive sample, which indicates that the sintering of the Ag NP ink is inhibited. The influence of the grain boundary diffusion coefficient (D^{gb}) in the sintering process of Ag NPs on the sintering aid layer is investigated via phase-field simulations. Without the sintering aid layer, the decreased temperature from 673 to 573 K leads to a substantial reduction to invalid in the grain boundary diffusion coefficient (i.e., $D^{gb}_{673K} > D^{gb}_{573K}$). As a result, sintering of Ag NPs occurs after diffusion evolution for 1 h at 673 K (Figure 2k), whereas no sintering necks are observed at 573 K (Figure 2l). As charge neutralization on the sintering aid layer increases the grain boundary diffusion coefficient of Ag NPs (i.e., $D^{gb}_{373K} > D^{gb}_{573K}$), sintering necks still form at a temperature of 373 K (Figure 2m), which supports the experimental results (Figures S14 and 15).

Because the cationic groups are needed for charge neutralization, additional nanoadditives have been chosen to demonstrate the concept, including metallic oxides (Al_2O_3 and MgO), salts ($CaCO_3$ and $BaTiO_3$), and metal (Cu) (Table S1). With cationic groups provided by metallic oxide (Al_2O_3 and MgO) and salt ($CaCO_3$ and $BaTiO_3$), the sintering temperature of Ag NPs of 50 nm significantly reduces on the coated paper. When the $CaCO_3$ nanoadditive is used in the sintering aid layer (Figure S16), the sintering temperature is further reduced to room temperature, although its exact mechanism of the performance enhancements over the other nanoadditives needs to be revealed in future studies. Although the sheet resistance of the sintered Ag patterns based on the sintering aid layer with TiO_2 nanoadditives at 120 °C and $CaCO_3$ nanoadditives at room temperature is slightly higher than those sintered at elevated temperatures (Figures S17 and S18), the values are comparable to those in the literature reports (Figure S5).[17,20,22,23,31−33] In contrast, when no nanoadditives or nanoadditives without cationic groups (e.g., Cu) are used in the sintering aid layers, the low-temperature sintering of Ag NP ink is not observed.

2.2. Integration and Demonstration of Various Biointegrated Sensing Modules. The integration of various sensing modules directly on the human skin surface involves the use of a simple, low-cost, and repeatable stamp-based transfer printing (Figure S19). In brief, dipping a soft elastomeric polymer shaped to the desired patterns on a wooden stamp into a commercial Ag NP ink picks up the Ag NPs on the patterned polymer. After coating the skin with the mixture of PVA paste and the $CaCO_3$ nanoadditive, bringing the inked stamp in contact with the skin, followed by pressing and retrieving of the stamp, leaves the patterned ink on the skin. A relatively hydrophilic surface of the sintering aid layer with different nanoadditives (Al_2O_3, MgO, $BaTiO_3$, TiO_2, $CaCO_3$, and Cu) (Figure S20) helps ensure a successful transfer printing process. Applying the air blower on the skin surface with ink patterns accelerates the evaporation of the solvents in the commercial Ag NP ink (i.e., reduced from several minutes to several seconds) to prepare the printed sensors on the skin. The drying process with the air blower (i.e., an electric hair dryer in this study) from a significantly large range of distances is relatively robust with a small variation in the sheet resistance of the obtained Ag patterns (Figure S21). As an alternative to the stamp-based transfer printing, extrusion of NP inks in an adaptive 3D printing process can also be exploited to directly fabricate skin-interfaced sensors on the moving human skin by real-time tracking of its rigid-body motion.[18]

https://dx.doi.org/10.1021/acsami.0c11479
ACS Appl. Mater. Interfaces XXXX, XXX, XXX−XXX

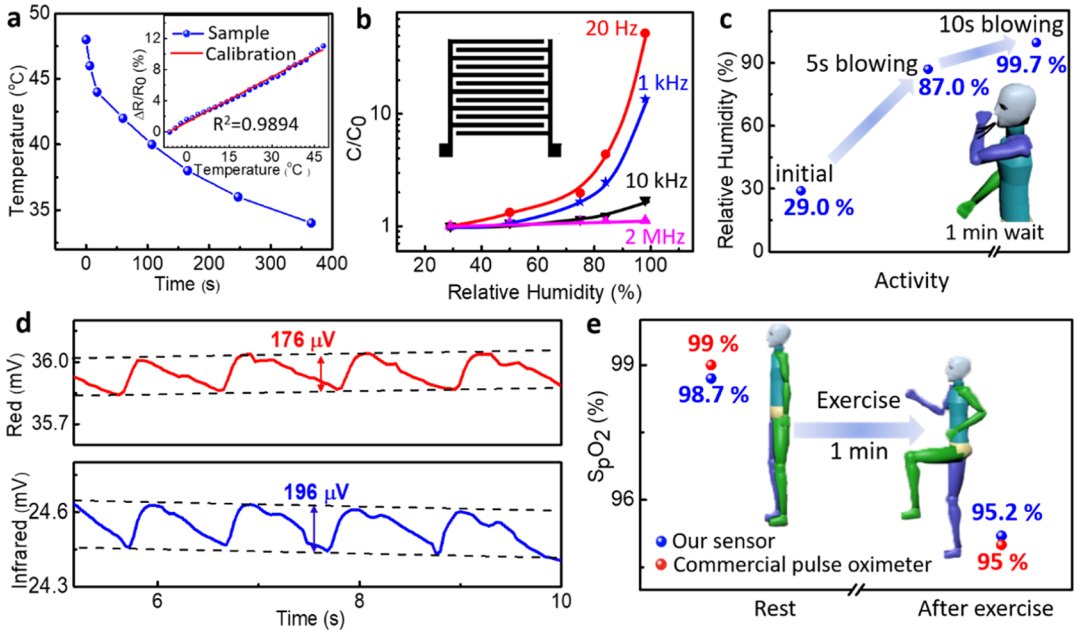

Figure 3. Design and demonstration of various on-body sensors to measure the temperature, humidity, and blood oxygen saturation. (a) Calibration of the temperature sensor indicates a linear dependence between the measured relative resistance change with the temperature from −5 to 50 °C. Cooling down of the skin from 50 °C to the room temperature highlights the sensing performance of the temperature sensor. (b) Dependence of the capacitance of the humidity sensor on the relative humidity at various frequencies (20 Hz, 1 kHz, 10 kHz, and 1 MHz). (c) Demonstration of the humidity sensor that measures the local moisture change after breathing out the moisturized air toward the sensors for 5 and 10 s. (d) Measured pulsating photoplethysmogram (PPG) voltage output signals from the photodetector for the red and infrared LEDs. (e) Measurements of human pulse rates and arterial blood oxygen saturation levels before and after an upward leg swinging exercise.

The proof-of-concept demonstration consists of temperature sensors, electrodes for electrophysiological (EP) signals, humidity sensors, and blood oximetry sensors (Figure S22). The sensing mechanism of the temperature sensor relies on the temperature-dependent resistance change that stronger vibration of the atoms at a higher temperature results in more electron collisions with reduced scattering time for the increased resistance. Characterization of temperature sensors with a manual/semiautomated probe system (FormFactor 11000) yields a linear dependence between the relative resistance change normalized by its initial value $\Delta R/R_0$ at the reference temperature T_0 and the temperature from −5 to 50 °C (Figure 3a, inset). Calculated from the slope of the calibration curve, the temperature coefficient of resistance α of the temperature sensor of 0.195%/°C is over 50% of its silver bulk counterpart (i.e., 0.38%/°C), consistent with literature reports.[43,44] The temperature sensor on the skin captures the local skin temperature increase caused by blowing hot air up to 50 °C, followed by cooling down to body temperature after removing the air blower (Figure 3a).

Skin hydration is another important indicator of human physiology to evaluate cosmetics and assess mental health. It is also related to thermoregulatory sweating and emotional sweating conditions to inform temperature control and emotion through the physiological and psychological processes.[45,46] The calibration of the hydration sensor against saturated salt solution at prescribed relative humidity relates its capacitance to the humidity at various frequencies (20 Hz, 1 kHz, 10 kHz, and 1 MHz) at a room temperature of 25 °C and an applied voltage of 1 V (Figure 3b). Besides a relative humidity of 29.0% in the ambient environment, saturated salt solutions of $Na_2Cr_2O_7$, NaCl, KCl, and Na_2HPO_4 provide relative humidities of 54, 75, 85, and 98%, respectively, in the sealed glass containers at the room temperature. Although the measured capacitance rapidly changes with the relative humidity at a lower frequency (e.g., 20 Hz and 1 kHz compared to 10 kHz and 2 MHz), the capacitance measurement at a lower frequency of 20 Hz also takes a much longer time before reaching equilibrium. Thus, the measurement at 1 kHz is selected for the on-body demonstration because of the relatively large response and quick measurement. The humidity sensor on the skin captures the local moisture change from slowly breathing out the moisture air toward the sensor for 5 and 10 s (Figure 3c). In addition to the direct comparison between the Ag-based sensors from this work and their commercial counterparts, the performance of our directly printed on-body temperature and humidity sensors compares favorably against those from literature reports in terms of their deposition technique, substrate material, and composite sensing materials (Table S3).

Measurements of the human pulse rate and arterial blood oxygen saturation rely on an optoelectronic sensor that consists of two LEDs with different peak emission wavelengths (e.g., red at 660 nm and infrared at 940 nm) and a single photodiode. Although the LEDs with a relatively larger size are selected in this proof-of-concept demonstration, they can be easily replaced by microscale LEDs (μ-LEDs) to further miniaturize the system.[24] The use of the Ag ink-based conductive pattern connects the two LEDs placed on the fingertip with the photodiode on the opposite side, which can be used to measure the tissue-mediated light transmission. Based on the measured periodic cycles with amplitudes of approximately 100−200 μV (Figure 3d), blood oxygen saturation (S_pO_2) is calculated to be ca. 98.7% with a pulse rate of 58 beats/min. A comparison with the measurements (60 beats/min, 99%) from a commercial finger pulse oximeter

https://dx.doi.org/10.1021/acsami.0c11479
ACS Appl. Mater. Interfaces XXXX, XXX, XXX−XXX

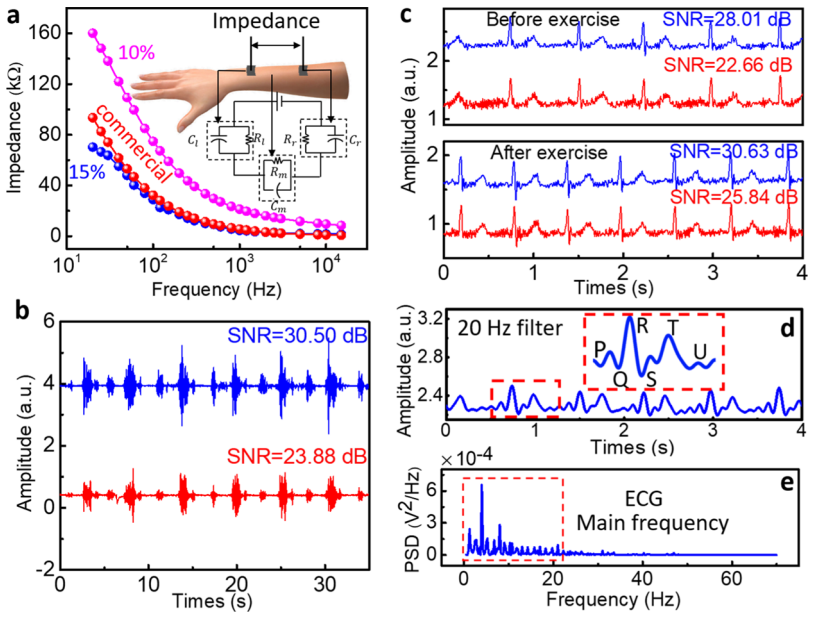

Figure 4. Design and demonstration of the Ag electrodes directly printed and room temperature-sintered on the human skin with enhanced contact quality to measure the EP signals such as ECG or EMG. (a) Impedance measurements as a function of frequency from two Ag electrodes of the same size separated by a given distance of 10 cm directly printed and room temperature-sintered on the human skin surface with the sintering aid layer. The inset shows the equivalent circuit model. (b) EMG and (c) ECG signals collected using the Ag electrodes on the sintering aid layer with 15 wt % PVA paste (blue) with a larger SNR than those from the commercial electrodes (red). (d) Applying a digital infinite impulse response (IIR) of 20 Hz to the ECG signal before exercise clearly identifies the clinically relevant P, QRS, T, and U waves. (e) PSD of the ECG indicates that the power is mostly below 20 Hz, where our electrodes show a much smaller contact impedance as measured in (a).

validates the results. Applying the pulse oximetry sensor on the fingertip of a healthy male young volunteer during an upward leg swinging exercise captures the decrease in S_pO_2 from 98.7 to 95.2% (Figure 3e, blue), as validated by the commercial device (Figure 3e, red). The pulse rate also increases from 58 to 76 beats/min, with amplitudes of red and infrared lights measured to be around 100 and 200 μV, respectively (Figure S23).

Coupling the electrodes on the skin surface through the sintering aid layer allows the capacitive sensing of the EP signals,[47,48] including ECG, EMG, or electroencephalogram (EEG). Capacitive sensing of EP signals involves measurements of electrical coupling between biological tissues and electrodes, mediated by the dielectric sintering aid layer. As the EP signal quality hinges on the contact impedance between the electrode and skin, the contact impedance is first characterized as a function of frequency. The electrode−skin interface is commonly modeled with a resistor R_i and a capacitor C_i (i = l or r for left and electrodes) in parallel.[49] By considering the equivalent resistor (R_m) and parasitic capacitor (C_m) of the human model between two electrodes (Figure 4a), the measured impedance between two electrodes can be written as

$$|Z| = [(R_l)^{-2} + (\omega C_l)^2]^{-1/2} + [(R_r)^{-2} + (\omega C_r)^2]^{-1/2}, + [(R_m)^{-2} + (\omega C_m)^2]^{-1/2}$$

where ω is the frequency. The electrode−skin contact impedances are often the leading terms with much larger contribution than the tissue impedance. Applying two electrodes of the same size separated by a given distance of 10 cm, the impedance measured from the Ag ink-based electrodes on the sintering aid layer is compared with that from the commercial gel electrodes. The impedance from our electrodes with 10 wt % PVA paste (magenta line) in the sintering aid layer is higher than that of the commercial gel electrodes (and thus worse EP signal quality in Figure S24). Because high impedance often causes increased noise at the low frequency, the lower interfacial impedance is desirable to ensure reliable EP signal acquisition.[50] As one of the major factors, the contact interface has a significant impact on the interfacial impedance. A significant reduction of impedance can be achieved with improved contact at the electrode−skin interface.[51] Furthermore, the increased viscosity of the sintering aid layer (termed as paste previously) improves the skin contact at the electrode−skin interface (with a reliable conductive pathway).[49] Therefore, the increased viscosity of the sintering aid layer is expected to result in decreased impedance for improved EP signal quality. In fact, the increase of the PVA powder from 10 wt % (purple) to 15 wt % (blue) in the PVA paste of the sintering aid layer reduces the impedance to be even smaller than that of the commercial gel electrodes (Figure 4a). In contrast to the impedance values of >100 kΩ from other studies,[52−54] the impedance of our Ag-based electrode sintered on the sintering aid layer with 15 wt % PVA paste is about 70 kΩ, which would lead to a higher signal-to-noise value and enhanced EP signal quality.

Using the sintering aid layer with 15 wt % PVA paste, high-fidelity EMG/ECG signals have been collected by the Ag ink electrodes (Figure 4bc, blue), with a larger signal-to-noise ratio (SNR) than those from the commercial electrodes (Figure 4bc, red). The measurements of EMG signals involve a series of muscle contractions from the arms of a healthy female volunteer, whereas the ECG signals are measured before and after running exercise. The ECG signals exhibit an increase in both amplitude and frequency, with the heart rate increased from 75 to 105 bpm after running exercise (Figure 4c). Applying a digital infinite impulse response (IIR) filter of 20 Hz to the ECG signal before exercise (Figure 4c, blue) clearly highlights the clinically relevant P, QRS, T, and U waves

https://dx.doi.org/10.1021/acsami.0c11479
ACS Appl. Mater. Interfaces XXXX, XXX, XXX−XXX

(Figure 4d). Power spectral density (PSD) of the ECG indicates that most of the power concentrates in the region below 20 Hz (Figure 4e). The smaller contact impedance from our sintering aid layer explains the improved high-fidelity ECG signals (Figure 4a).

The integration of these directly printed on-body sensors with the FPCB in a fully passive operating mode (i.e., without the battery) also allows for wireless detection of their sensing signals. After determining the read range from the SL900A chip as a function of the working frequency (Figure S25a), 882 MHz is selected in the wireless measurements. When operated at 882 MHz, the temperature (Figure S25b) and humidity (Figure S25c) can be wirelessly measured with high precision and accuracy from a distance of 30 cm. In addition to the fully passive mode, the SL900A can be assisted by a paper-based battery to work in the semi-passive mode. The use of a battery can further increase the communication range with the reader and enable data logging. Nevertheless, the simple demonstration illustrated here showcases the feasibility of fabricating the FPCBs with the proposed method, which may also be applied to more complicated FPCBs[55−57] in future studies. Furthermore, the high-fidelity ECG signals can also be wirelessly captured. Without the complicated paper-based FPCB, a commercial wireless module with a small footprint is used here to further capture the ECG signals wirelessly (Figure S25d).

2.3. Demonstration of Sensing Module Removal and Disposal. As future wide adoption of wearable devices would lead to electronic wastes, proper disposal of these devices starts to gain momentum, especially considering the recent development of transient electronics in the past decade.[58,59] Toward this end, the aforementioned on-body sensors are also demonstrated to be suitable for easy removal and disposal (Figure 5). Peeling off the thin-film device from the skin removes the device with negligible effects on the skin (Figure 5b). The skin texture on the back surface of the thin film highlights the excellent adhesion between the device and skin. Although the thin-film device remains relatively stable at room temperature in water for over 2 h [Figure 5a(i)], decomposition begins after the temperature increases above 60 °C [Figure 5a(ii)] and dissolves completely after stirring for 5 min [Figure 5a(iii)]. Because of the water solubility of the PVA powder in the sintering aid layer at elevated temperature, washing hands in warm water flow conveniently removes the device from the skin (Figure 5c). The materials exploited in the device system are biocompatible with minimal toxicity, which enables their use for green electronics, biointegrated electronics, or even implantable devices. For instance, PVA powder and $CaCO_3$ are commonly used in a variety of medical applications because of their biocompatibility and low toxicity.[60,61] Ag NPs with low mammalian cytotoxicity and antibacterial properties become common additives for applications in catalysis, tissue/tumor imaging, biosensing, and drug delivery. Additionally, the PVP-coated Ag NPs can effectively block the transmission of cell-free and cell-associated HIV-1, although a high dose of 0.6 mg/mL does not cause acute inflammatory and cell death.[62]

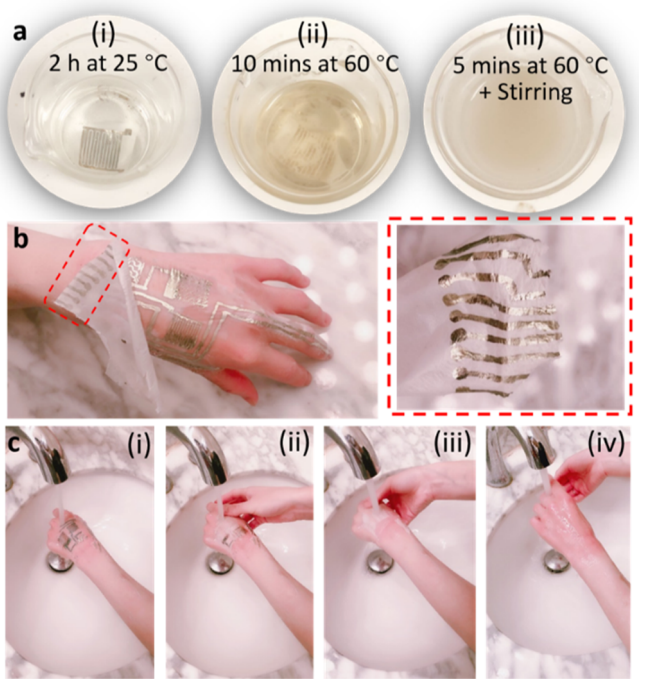

Figure 5. Removal and disposal demonstration of the on-body sensors. (a) Optical images of the thin-film on-body sensors show the sequence of device dissolution: (i) stable in water at room temperature, (ii) initiation of the decomposition above 60 °C, and (iii) completely dissolved after stirring for 5 min. (b) Peeling off the on-body sensing film with negligible effects on the skin conveniently removes the device. (c) Sequence of optical images shows easy removal of the device from the skin by washing hands in warm water flow.

3. CONCLUSIONS

In summary, we have reported the design and demonstration of a simple yet universal manufacturing approach to fabricate and integrate paper/fabric-based FPCBs at low temperature and multifunctional on-body sensors directly on the human skin at room temperature for a soft body area sensor network. The fabrication scheme relies on a sintering aid layer consisting of the PVA paste and nanoadditives (e.g., TiO_2 or $CaCO_3$, among others). Using the sintering aid layer on various paper/fabric substrates or the human skin, the sintering temperature of metal NPs is significantly reduced even to room temperature. The conductive metal pattern sintered at the metal/sintering aid layer interface has an ultrathin geometry, leading to an excellent electromechanical performance of the resulting devices against bending and folding for origami/kirigami applications. When applying the same fabrication scheme to integrate metal patterns on the fabric substrate, the resulting device with a robust performance in the water or moisture environment (>100 h) enables the application in biointegrated electronics during sweating. Moreover, printing and room-temperature sintering of metal NP ink directly on the human skin surface demonstrate the extended capability of the fabrication scheme to prepare various on-body sensors for physiological signal monitoring. The demonstrated high-performance sensors could precisely and continuously capture temperature, humidity, or local moisture change, blood oxygen saturation, and EP signals such as EMG/ECG. With enhanced signal quality and improved performance over those from their commercial counterparts, these proof-of-the-concept sensors with other expanded modules provide a repertoire of wearable electronics for health monitoring. Additionally, the system with demonstrated modules of on-body sensors for physiological signal monitoring and FPCBs for wireless transmission can be potentially applied to signal progression and severity in COVID-19 patients.

https://dx.doi.org/10.1021/acsami.0c11479
ACS Appl. Mater. Interfaces XXXX, XXX, XXX−XXX

4. EXPERIMENTAL SECTION

4.1. Materials. The metal micro/nanoparticles (MPs/NPs), including Ag NPs of ~50 nm, Ag MPs of ~2 or ~40 μm, Ni NPs of ~100 nm, Ni NPs of ~50 nm, and Cu MPs of ~1 μm, all with a purity of 99.9%, were purchased from Shanghai Aladdin. Polyvinylpyrrolidone (PVP-K30), $AgNO_3$ (99.99% metals basis), hydrazine hydrate (80%), and L-ascorbic acid (99.0%) were purchased from Shanghai Aladdin. Polyvinyl alcohol (PVA) powder (molecular weight: 89,000−98,000; 99+% hydrolyzed), titanium dioxide (TiO_2) with a particle diameter of 20−50 nm, and calcium carbonate ($CaCO_3$) with a particle diameter of 20−50 nm were purchased from Sigma-Aldrich, USA. Other nanoadditives (i.e., Al_2O_3 particles of ~50 nm, MgO particles of ~50 nm, and $BaTiO_3$ particles of ~50 nm), all with a purity of 99.9%, were purchased from Shanghai Aladdin.

4.2. Preparation of the Inks with Ni/Ag Core/Shell NPs and Other NPs. Ni/Ag core/shell NPs were prepared by hydrazine reduction of $AgNO_3$ in deionized water with PVP as the protective agent. First, 1.7 g of $AgNO_3$, 1.7 g of PVP, and 180 g of deionized water were added to a 300 mL beaker with a mechanical stirrer. Next, 1.17 g of 50 nm Ni NPs was added into the dispersion. The calculation indicates that 1.7 g of $AgNO_3$ would require 0.46 g of hydrazine hydrate to be fully reduced. However, a minimized use of the hydrazine hydrate is desired because of its toxicity. By considering the possible inhomogeneous dispersion, we added 0.8 g of hydrazine hydrate into the Ni NP−PVP/$AgNO_3$ solution for the reduction reaction. After about 0.5 h, the reaction products were separated by centrifuging at 4000 rpm for 5 min. The obtained Ni/Ag core/shell NPs were further purified with centrifuging separation and redispersion in pure ethyl alcohol for three cycles. Dissolving the commercial or obtained metal particles in glycol at a mass ratio of 1:4 yielded a high-quality metal particle ink.

4.3. Preparation of the Sintering Aid Layer. The PVA paste was prepared by mixing the PVA powder with deionized water at different weight ratios: 10, 15, or 20 wt % (i.e., PVA powder/deionized water = 1:9, 3:17, or 1:4), followed by stirring at 70 °C to yield a viscous, transparent solution. The solution of the sintering aid layer was prepared by adding the nanoadditives into the PVA paste with continuous stirring at 700 rpm at 70 °C for a homogeneous mixture. For the TiO_2 nanoadditive, it was added to the 10 wt % PVA paste at weight ratios of 1:20, 1:15, 1:10, and 1:5 for TiO_2 to PVA paste. As for the $CaCO_3$ nanoadditive, it was added to the 10 or 15 wt % PVA paste at a weight ratio of 1:10 for $CaCO_3$ to PVA paste. After coating the sintering aid layer solution on the paper or skin, it was kept to yield the sintering aid layer, by drying in atmospheric air at room temperature unless specified otherwise.

4.4. Demonstration of the Effect of the Cationic Radical on the Sintering of Ag NPs. First, 1 g of PVA powder and 9 g of deionized water were added to a 25 mL beaker, followed by stirring at 70 °C to yield a viscous, transparent solution (Figure S13a). Next, 10 g of L-ascorbic acid was added to the obtained solution, resulting in a color change of the solution from transparent to white (Figure S13b). After stirring for about 3 min, the solution changed back to transparent (Figure S13c). Next, 1 g of TiO_2 was added to the mixture with continuous stirring for 15 min to yield the ivory mixture (Figure S13d). After coating this sintering aid layer on the paper, the Ag NP ink was inkjet-printed and annealed at a temperature of 120 °C. The obtained sample was observed to be nonconductive (Figure S13e).

4.5. Preparation of the Paper-Based FPCB. The Ag NP ink was first inkjet-printed on the coated paper as conductive lines with contact pads (0.4 mm × 0.355 mm with a spacing of 0.8 mm between pads) in the FPCB. Next, the SL900A package (5 mm × 5 mm × 0.9 mm) was mounted onto the paper with conductive Ag patterns, where the anisotropic conductive paste was used to connect the chip and the Ag pads to result in the paper-based FPCB.

4.6. Phase-Field Simulation of Particle Sintering. The microstructural evolution is driven by the minimization of the free energy function F that is defined as

$$F = \int_v \left\{ f(c, \eta_\alpha) + \frac{1}{2}\kappa_c \left| \nabla c \right|^2 + \frac{1}{2}\sum_{\alpha=1}^{N} \kappa_\eta |\nabla \eta_\alpha|^2 \right\} \mathrm{d}v \quad (1)$$

where the conserved field parameter c describes the Ag concentration field, the nonconserved order parameter η_α describes the morphological evolution of the particles, α is the index of a particle, and f is the local bulk chemical free energy function. κ_c and κ_η are the gradient energy parameters for the conserved and nonconserved fields, respectively.[63] N is the total number of the order parameter.

The conserved field c can be written as

$$\frac{\partial c}{\partial t} = \nabla \cdot \left(M \cdot \nabla \frac{\delta F}{\delta c(x, t)} \right) \quad (2)$$

where x is the spatial position vector, t is the time, and M is the concentration mobility tensor that can be expressed as

$$M = D / \left. \frac{\partial^2 F}{\partial c^2} \right|_{c=1} \quad (3)$$

The diffusivity tensor D in eq 3 can be defined as

$$D = D^{\mathrm{v}} + D^{\mathrm{s}} + D^{\mathrm{gb}} \quad (4)$$

where D^{v}, D^{s}, and D^{gb} are the diffusivity tensors of volume, surface, and grain boundary, respectively. Because the contribution of the volume diffusion is negligible and the surface diffusion is only present on the surface of the particle, the grain boundary diffusion is the leading factor in the sintering at the interface between two particles. The grain boundary diffusion is proportional to the grain boundary diffusion coefficient $D^{\mathrm{gb}}_{\mathrm{eff}}$, which is valid for the sintering temperature above 573 K (e.g., $D^{\mathrm{gb}}_{873\mathrm{K}}$). As the sintering temperature reduces to be below 573 K, the grain boundary diffusion coefficient ($D^{\mathrm{gb}}_{573\mathrm{K}}$) tends to approach the volume diffusion coefficient, leading to the unsintered NPs. As the sintering aid layer increases the grain boundary diffusion coefficient at a temperature of 373 K ($D^{\mathrm{gb}}_{373\mathrm{K}}$), the sintering of Ag NPs occurs with sintering necks formed. Here, all of these parameters in the phase-field model are consistent with the literature reports.[64,65]

4.7. Preparation of Saturated Salt Solutions. The $Na_2Cr_2O_7$, NaCl, KCl, and Na_2HPO_4 salts were dissolved in glass containers of 4 L at 60 °C. Cooling down the solutions to the room temperature yielded saturated salt solutions with precipitation. Sealing the obtained solutions at room temperature prepared them for use later.

4.8. Drying Process with the Electric Hair Dryer. The electric hair dryer was used as the air blower to dry the Ag pattern printed on the skin via the stamp-based transfer process. The distance between the air outlet of the hair dryer and the skin surface was about 1−2 cm. The blower was set at the position of full power at medium temperature (i.e., room temperature) for quick drying of about 20 s. The electric hair dryer with a power of 1875 Watts could produce an airspeed of 40 mph (measured at a couple of inches away from the outlet). When the Ag ink patterns were dried using the hair dryer at different distances from the outlet (i.e., ~1, ~5, ~10, and ~20 cm), it took the hair dryer a longer time to dry the patterns (~20, ~45, ~60, and ~120 s) as the distance was progressively increased. The sheet resistance of the dried Ag patterns was observed to be slightly different (~14, ~20, ~32, and 28 μΩ cm), but the difference was much smaller with a small variation in the distance and could also be easily accounted for in the calibration of the sensors.

4.9. Calculation of Blood Oxygen Saturation (S_pO_2). Calculation of S_pO_2 was based on the photodiffusion analysis and the modified Lamber−Beer equation[66]

$$\mathrm{Sp\,O_2}(t) = \frac{\varepsilon_{\mathrm{Hb}}(\lambda_{\mathrm{R}})\mathrm{DPF}_{\mathrm{R-IR}} - \varepsilon_{\mathrm{Hb}}(\lambda_{\mathrm{IR}})R(t)}{[\varepsilon_{\mathrm{Hb}}(\lambda_{\mathrm{R}}) - \varepsilon_{\mathrm{HbO_2}}(\lambda_{\mathrm{R}})]\mathrm{DPF}_{\mathrm{R-IR}} + [\varepsilon_{\mathrm{HbO_2}}(\lambda_{\mathrm{IR}}) - \varepsilon_{\mathrm{Hb}}(\lambda_{\mathrm{IR}})]R(t)} \quad (5)$$

where $\varepsilon_{\mathrm{HbO_2}}(\lambda_{\mathrm{R}})$ and $\varepsilon_{\mathrm{HbO_2}}(\lambda_{\mathrm{IR}})$ [or $\varepsilon_{\mathrm{Hb}}(\lambda_{\mathrm{R}})$ and $\varepsilon_{\mathrm{Hb}}(\lambda_{\mathrm{IR}})$] are the extinction coefficients of oxyhemoglobin (or deoxyhemoglobin) for the red and infrared light with wavelengths of 640 and 950 nm,

https://dx.doi.org/10.1021/acsami.0c11479
ACS Appl. Mater. Interfaces XXXX, XXX, XXX−XXX

respectively. The quantity DPF_{R-IR} is the influence coefficient of the dissimilar optical path lengths at the two wavelengths. These parameters have been determined[66] to be $\varepsilon_{HbO_2}(\lambda_R) = 0.011\ mm^{-1}$, $\varepsilon_{Hb}(\lambda_R) = 0.106\ mm^{-1}$, $\varepsilon_{HbO_2}(\lambda_{IR}) = 0.028\ mm^{-1}$, $\varepsilon_{Hb}(\lambda_{IR}) = 0.018\ mm^{-1}$, and $DPF_{R-IR} = 1.4$. Applying the same values for these parameters as in the literature report,[66] eq 5 can be simplified to

$$Sp\ O_2(t) = \frac{0.1484 - 0.018 \times R(t)}{0.133 + 0.01 \times R(t)} \quad (6)$$

where the ratio $R(t)$ between the red and the infrared pulsatile components can be expressed as

$$R = \frac{I_{AC}^{\lambda_R}}{I_{DC}^{\lambda_R}} / \frac{I_{AC}^{\lambda_{IR}}}{I_{DC}^{\lambda_{IR}}} \quad (7)$$

In eq 7, the alternating current component I_{AC} is the difference between the peaks and troughs of the pulse wave, whereas the direct current component I_{DC} is the mean value.

■ ASSOCIATED CONTENT

Supporting Information

The Supporting Information is available free of charge at https://pubs.acs.org/doi/10.1021/acsami.0c11479.

Details on the materials, experimental procedures, designs of paper-based FPCB using the SL900A chip, pattern designs of sensors and characterization results of the contact angle, AFM, XRD, SEM, sheet resistance, PPG voltage measuring, and EMG/ECG signal testing (PDF)

■ AUTHOR INFORMATION

Corresponding Authors

Peng He − *State Key Laboratory of Advanced Welding & Joining, Harbin Institute of Technology, Shenzhen 518055, People's Republic of China*; Email: hithepeng@hit.edu.cn

Weiwei Zhao − *State Key Laboratory of Advanced Welding & Joining, Flexible Printed Electronics Technology Center, and The School of Material Science and Engineering, Harbin Institute of Technology, Shenzhen 518055, People's Republic of China*; orcid.org/0000-0002-0373-1146; Email: wzhao@hit.edu.cn

Huanyu Cheng − *Department of Engineering Science and Mechanics and Department of Materials Science and Engineering, The Pennsylvania State University, University Park, Pennsylvania 16802, United States*; orcid.org/0000-0001-6075-4208; Email: Huangyu.Cheng@psu.edu

Authors

Ling Zhang − *State Key Laboratory of Advanced Welding & Joining and Flexible Printed Electronics Technology Center, Harbin Institute of Technology, Shenzhen 518055, People's Republic of China; Department of Engineering Science and Mechanics, The Pennsylvania State University, University Park, Pennsylvania 16802, United States*

Hongjun Ji − *State Key Laboratory of Advanced Welding & Joining, Flexible Printed Electronics Technology Center, and The School of Material Science and Engineering, Harbin Institute of Technology, Shenzhen 518055, People's Republic of China*; orcid.org/0000-0002-4159-6838

Houbing Huang − *Advanced Research Institute of Multidisciplinary Science, Beijing Institute of Technology, Beijing 100081, China*

Ning Yi − *Department of Materials Science and Engineering, The Pennsylvania State University, University Park, Pennsylvania 16802, United States*; orcid.org/0000-0002-4116-5202

Xiaoming Shi − *Advanced Research Institute of Multidisciplinary Science, Beijing Institute of Technology, Beijing 100081, China*

Senpei Xie − *Flexible Printed Electronics Technology Center and The School of Material Science and Engineering, Harbin Institute of Technology, Shenzhen 518055, People's Republic of China*

Yaoyin Li − *Flexible Printed Electronics Technology Center and The School of Material Science and Engineering, Harbin Institute of Technology, Shenzhen 518055, People's Republic of China*

Ziheng Ye − *The School of Material Science and Engineering, Harbin Institute of Technology, Shenzhen 518055, People's Republic of China*

Pengdong Feng − *Flexible Printed Electronics Technology Center and The School of Material Science and Engineering, Harbin Institute of Technology, Shenzhen 518055, People's Republic of China*; orcid.org/0000-0002-8066-3490

Tiesong Lin − *State Key Laboratory of Advanced Welding & Joining, Harbin Institute of Technology, Shenzhen 518055, People's Republic of China*; orcid.org/0000-0002-7454-3142

Xiangli Liu − *The School of Material Science and Engineering, Harbin Institute of Technology, Shenzhen 518055, People's Republic of China*

Xuesong Leng − *State Key Laboratory of Advanced Welding & Joining, Harbin Institute of Technology, Shenzhen 518055, People's Republic of China*

Mingyu Li − *State Key Laboratory of Advanced Welding & Joining, Flexible Printed Electronics Technology Center, and The School of Material Science and Engineering, Harbin Institute of Technology, Shenzhen 518055, People's Republic of China*; orcid.org/0000-0002-3102-1328

Jiaheng Zhang − *State Key Laboratory of Advanced Welding & Joining, Flexible Printed Electronics Technology Center, and The School of Material Science and Engineering, Harbin Institute of Technology, Shenzhen 518055, People's Republic of China*; orcid.org/0000-0002-2377-9796

Xing Ma − *State Key Laboratory of Advanced Welding & Joining, Flexible Printed Electronics Technology Center, and The School of Material Science and Engineering, Harbin Institute of Technology, Shenzhen 518055, People's Republic of China*; orcid.org/0000-0002-2248-4806

Complete contact information is available at: https://pubs.acs.org/10.1021/acsami.0c11479

Author Contributions

L.Z., H.J., H.H., and N.Y. contributed equally. L.Z, W.Z, and H.C. led the development of the concepts, designed the experiments, and interpreted the results. L.Z., H.J., N.Y., S.X., Y.L., Z.Y., and P.F. performed the experimental measurements. L.Z., H.H., and X.S. performed phase-field simulation. L.Z., T.L., X.L., X.L., M.L., J.Z., X.M., and P.H. helped analyze the data. L.Z. and H.C. wrote the paper.

Notes

The authors declare no competing financial interest.

■ ACKNOWLEDGMENTS

This work was supported by several grants provided by The Pennsylvania State University and the National Science

Foundation (NSF) (grant no. ECCS-1933072) to H.C. and the Shenzhen Science and Technology Program (grant no. KQTD20170809110344233, JCYJ20170811160129498) and Bureau of Industry and Information Technology of Shenzhen through the Graphene Manufacturing Innovation Center (201901161514). X.L. acknowledges the support from the Natural Science Foundation of China (11672090).

REFERENCES

(1) Kim, K.; Kim, B.; Lee, C. H. Printing Flexible and Hybrid Electronics for Human Skin and Eye-Interfaced Health Monitoring Systems. *Adv. Mater.* **2020**, *32*, 1902051.

(2) Dervisevic, M.; Alba, M.; Prieto-Simon, B.; Voelcker, N. H. Skin in the Diagnostics Game: Wearable Biosensor Nano-and Microsystems for Medical Diagnostics. *Nano Today* **2020**, *30*, 100828.

(3) Zheng, Y.; He, Z.; Gao, Y.; Liu, J. Direct Desktop Printed-Circuits-on-Paper Flexible Electronics. *Sci. Rep.* **2013**, *3*, 1786.

(4) Buechley, L.; Eisenberg, M. Fabric Pcbs, Electronic Sequins, and Socket Buttons: Techniques for E-Textile Craft. *Personal Ubiquitous Comput.* **2009**, *13*, 133−150.

(5) Ahn, J.; Seo, J.-W.; Lee, T.-I.; Kwon, D.; Park, I.; Kim, T.-S.; Lee, J.-Y. Extremely Robust and Patternable Electrodes for Copy-Paper-Based Electronics. *ACS Appl. Mater. Interfaces* **2016**, *8*, 19031−19037.

(6) Liu, H.; Jiang, H.; Du, F.; Zhang, D.; Li, Z.; Zhou, H. Flexible and Degradable Paper-Based Strain Sensor with Low Cost. *ACS Sustainable Chem. Eng.* **2017**, *5*, 10538−10543.

(7) Kanaparthi, S.; Badhulika, S. Solvent-Free Fabrication of a Biodegradable All-Carbon Paper Based Field Effect Transistor for Human Motion Detection through Strain Sensing. *Green Chem.* **2016**, *18*, 3640−3646.

(8) Ershad, F.; Thukral, A.; Yue, J.; Comeaux, P.; Lu, Y.; Shim, H.; Sim, K.; Kim, N.-I.; Rao, Z.; Guevara, R.; Contreras, L.; Pan, F.; Zhang, Y.; Guan, Y.-S.; Yang, P.; Wang, X.; Wang, P.; Wu, X.; Yu, C. Ultra-Conformal Drawn-on-Skin Electronics for Multifunctional Motion Artifact-Free Sensing and Point-of-Care Treatment. *Nat. Commun.* **2020**, *11*, 3823.

(9) Xu, Y.; Zhao, G.; Zhu, L.; Fei, Q.; Zhang, Z.; Chen, Z.; An, F.; Chen, Y.; Ling, Y.; Guo, P.; Ding, S.; Huang, G.; Chen, P.-Y.; Cao, Q.; Yan, Z. Pencil-paper on-skin electronics. *Proc. Natl. Acad. Sci.* **2020**, *117*, 18292−18301.

(10) Yang, Z.; Zhang, Y.; Itoh, T.; Maeda, R. Flexible Implantable Microtemperature Sensor Fabricated on Polymer Capillary by Programmable Uv Lithography with Multilayer Alignment for Biomedical Applications. *J. Microelectromech. Syst.* **2014**, *23*, 21−29.

(11) Lee, J.; Kim, S.; Lee, J.; Yang, D.; Park, B. C.; Ryu, S.; Park, I. A Stretchable Strain Sensor Based on a Metal Nanoparticle Thin Film for Human Motion Detection. *Nanoscale* **2014**, *6*, 11932−11939.

(12) Wang, C.-T.; Huang, K.-Y.; Lin, D. T. W.; Liao, W.-C.; Lin, H.-W.; Hu, Y.-C. A Flexible Proximity Sensor Fully Fabricated by Inkjet Printing. *Sensors* **2010**, *10*, 5054−5062.

(13) Cai, L.; Zhang, S.; Zhang, Y.; Li, J.; Miao, J.; Wang, Q.; Yu, Z.; Wang, C. Direct Printing for Additive Patterning of Silver Nanowires for Stretchable Sensor and Display Applications. *Adv. Mater. Technol.* **2018**, *3*, 1700232.

(14) Lee, J.; Kwon, H.; Seo, J.; Shin, S.; Koo, J. H.; Pang, C.; Son, S.; Kim, J. H.; Jang, Y. H.; Kim, D. E.; Lee, T. Conductive Fiber-Based Ultrasensitive Textile Pressure Sensor for Wearable Electronics. *Adv. Mater.* **2015**, *27*, 2433−2439.

(15) Trung, T. Q.; Ramasundaram, S.; Hwang, B.-U.; Lee, N.-E. An All-Elastomeric Transparent and Stretchable Temperature Sensor for Body-Attachable Wearable Electronics. *Adv. Mater.* **2016**, *28*, 502−509.

(16) Russo, A.; Ahn, B. Y.; Adams, J. J.; Duoss, E. B.; Bernhard, J. T.; Lewis, J. A. Pen-on-Paper Flexible Electronics. *Adv. Mater.* **2011**, *23*, 3426−3430.

(17) Tai, Y.-L.; Yang, Z.-G. Fabrication of Paper-Based Conductive Patterns for Flexible Electronics by Direct-Writing. *J. Mater. Chem.* **2011**, *21*, 5938−5943.

(18) Zhu, Z.; Guo, S.-Z.; Hirdler, T.; Eide, C.; Fan, X.; Tolar, J.; McAlpine, M. C. 3d Printed Functional and Biological Materials on Moving Freeform Surfaces. *Adv. Mater.* **2018**, *30*, 1707495.

(19) Frutiger, A.; Muth, J. T.; Vogt, D. M.; Mengüç, Y.; Campo, A.; Valentine, A. D.; Walsh, C. J.; Lewis, J. A. Capacitive Soft Strain Sensors via Multicore-Shell Fiber Printing. *Adv. Mater.* **2015**, *27*, 2440−2446.

(20) Xu, L. Y.; Yang, G. Y.; Jing, H. Y.; Wei, J.; Han, Y. D. Pressure-Assisted Low-Temperature Sintering for Paper-Based Writing Electronics. *Nanotechnology* **2013**, *24*, 355204.

(21) Li, J.; Mao, P.; Wang, F. *16th International Conference on Electronic Packaging Technology (ICEPT)*; IEEE, 2015; pp 985−988.

(22) Gaspar, C.; Passoja, S.; Olkkonen, J.; Smolander, M. Ir-Sintering Efficiency on Inkjet-Printed Conductive Structures on Paper Substrates. *Microelectron. Eng.* **2016**, *149*, 135−140.

(23) Hou, L.; Zhao, H.; Lu, Y. Fabrication of User-Defined Copper Conductive Patterns onto Paper Substrate for Flexible Electronics by Combining Wax Patterning with Electroless Plating. *J. Mater. Sci.: Mater. Electron.* **2017**, *28*, 4219−4228.

(24) Kim, J.; Salvatore, G. A.; Araki, H.; Chiarelli, A. M.; Xie, Z.; Banks, A.; Sheng, X.; Liu, Y.; Lee, J. W.; Jang, K.-I.; Heo, S. Y.; Cho, K.; Luo, H.; Zimmerman, B.; Kim, J.; Yan, L.; Feng, X.; Xu, S.; Fabiani, M.; Gratton, G.; Huang, Y.; Paik, U.; Rogers, J. A. Battery-Free, Stretchable Optoelectronic Systems for Wireless Optical Characterization of the Skin. *Sci. Adv.* **2016**, *2*, No. e1600418.

(25) Niu, S.; Matsuhisa, N.; Beker, L.; Li, J.; Wang, S.; Wang, J.; Jiang, Y.; Yan, X.; Yun, Y.; Burnett, W.; Poon, A. S. Y.; Tok, J. B.-H.; Chen, X.; Bao, Z. A Wireless Body Area Sensor Network Based on Stretchable Passive Tags. *Nat. Electron.* **2019**, *2*, 361−368.

(26) Mahajan, A.; Francis, L. F.; Frisbie, C. D. Facile Method for Fabricating Flexible Substrates with Embedded, Printed Silver Lines. *ACS Appl. Mater. Interfaces* **2014**, *6*, 1306−1312.

(27) Barr, M. C.; Rowehl, J. A.; Lunt, R. R.; Xu, J.; Wang, A.; Boyce, C. M.; Im, S. G.; Bulović, V.; Gleason, K. K. Direct Monolithic Integration of Organic Photovoltaic Circuits on Unmodified Paper. *Adv. Mater.* **2011**, *23*, 3500−3505.

(28) Hyun, W. J.; Park, O. O.; Chin, B. D. Foldable Graphene Electronic Circuits Based on Paper Substrates. *Adv. Mater.* **2013**, *25*, 4729−4734.

(29) Siegel, A. C.; Phillips, S. T.; Dickey, M. D.; Lu, N.; Suo, Z.; Whitesides, G. M. Foldable Printed Circuit Boards on Paper Substrates. *Adv. Funct. Mater.* **2010**, *20*, 28−35.

(30) Zhang, L.; Feng, P.; Xie, S.; Wang, Y.; Ye, Z.; Fu, Z.; Wang, Q.; Ma, X.; Zhang, J.; He, P.; Li, K.; Zhao, W. Low-Temperature Sintering of Silver Nanoparticles on Paper by Surface Modification. *Nanotechnology* **2019**, *30*, 505303.

(31) Li, W.; Chen, M.; Li, W.; You, C.; Wei, J.; Zhi, L. Synthesis of Air Stable Silver Nanoparticles and Their Application as Conductive Ink on Paper Based Flexible Electronics. *Mater. Res. Innovat.* **2014**, *18*, S4.

(32) Li, W.; Li, W.; Wang, M.; Liu, G.; Chen, M. Direct writing of stable Cu-Ag-based conductive patterns for flexible electronics. *RSC Adv.* **2016**, *6*, 10670−10676.

(33) Bhat, K. S.; Ahmad, R.; Wang, Y.; Hahn, Y.-B. Low-Temperature Sintering of Highly Conductive Silver Ink for Flexible Electronics. *J. Mater. Chem. C* **2016**, *4*, 8522−8527.

(34) Bandodkar, A. J.; Hung, V. W. S.; Jia, W.; Valdés-Ramírez, G.; Windmiller, J. R.; Martinez, A. G.; Ramírez, J.; Chan, G.; Kerman, K.; Wang, J. Tattoo-Based Potentiometric Ion-Selective Sensors for Epidermal Ph Monitoring. *Analyst* **2013**, *138*, 123−128.

(35) Hwang, S.-W.; Kim, D.-H.; Tao, H.; Kim, T.-i.; Kim, S.; Yu, K. J.; Panilaitis, B.; Jeong, J.-W.; Song, J.-K.; Omenetto, F. G.; Rogers, J. A. Materials and Fabrication Processes for Transient and Bioresorbable High-Performance Electronics. *Adv. Funct. Mater.* **2013**, *23*, 4087−4093.

(36) Kang, S.-K.; Hwang, S.-W.; Cheng, H.; Yu, S.; Kim, B. H.; Kim, J.-H.; Huang, Y.; Rogers, J. A. Dissolution Behaviors and Applications of Silicon Oxides and Nitrides in Transient Electronics. *Adv. Funct. Mater.* **2014**, *24*, 4427−4434.

https://dx.doi.org/10.1021/acsami.0c11479
ACS Appl. Mater. Interfaces XXXX, XXX, XXX−XXX

(37) Porstendörfer, J. Die Diffusionskoeffizienten Und Mittleren Freien Weglängen Der Geladenen Und Neutralen Radon-Folgeprodukte in Luft. *Z. Phys.* **1968**, *213*, 384−396.
(38) Magdassi, S.; Grouchko, M.; Berezin, O.; Kamyshny, A. Triggering the Sintering of Silver Nanoparticles at Room Temperature. *ACS Nano* **2010**, *4*, 1943−1948.
(39) Filippo, E.; Carlucci, C.; Capodilupo, A. L.; Perulli, P.; Conciauro, F.; Corrente, G. A.; Gigli, G.; Ciccarella, G. Facile preparation of TiO2-polyvinyl alcohol hybrid nanoparticles with improved visible light photocatalytic activity. *Appl. Surf. Sci.* **2015**, *331*, 292−298.
(40) Kettle, J.; Lamminmäki, T.; Gane, P. A Review of Modified Surfaces for High Speed Inkjet Coating. *Surf. Coat. Technol.* **2010**, *204*, 2103−2109.
(41) Ahmad, J.; Deshmukh, K.; Hägg, M. B. Influence of TiO2on the Chemical, Mechanical, and Gas Separation Properties of Polyvinyl Alcohol-Titanium Dioxide (PVA-TiO2) Nanocomposite Membranes. *Int. J. Polym. Anal. Charact.* **2013**, *18*, 287−296.
(42) Hadi, A.; Hashim, A.; Al-Khafaji, Y. Structural, Optical and Electrical Properties of Pva/Peo/Sno 2 New Nanocomposites for Flexible Devices. *Trans. Electr. Electron. Mater.* **2020**, *21*, 283.
(43) Dankoco, M. D.; Tesfay, G. Y.; Benevent, E.; Bendahan, M. Temperature Sensor Realized by Inkjet Printing Process on Flexible Substrate. *Mater. Sci. Eng., B* **2016**, *205*, 1−5.
(44) Mattana, G.; Kinkeldei, T.; Leuenberger, D.; Ataman, C.; Ruan, J. J.; Molina-Lopez, F.; Quintero, A. V.; Nisato, G.; Tröster, G.; Briand, D.; Rooij, N. F. Woven Temperature and Humidity Sensors on Flexible Plastic Substrates for E-Textile Applications. *IEEE Sens. J.* **2013**, *13*, 3901−3909.
(45) Baker, L. B. Physiology of Sweat Gland Function: The Roles of Sweating and Sweat Composition in Human Health. *Temperature* **2019**, *6*, 211−259.
(46) Schlereth, T.; Dieterich, M.; Birklein, F. Hyperhidrosis—Causes and Treatment of Enhanced Sweating: In reply. *Deutsches Ärzteblatt Int.* **2009**, *106*, 448.
(47) Jeong, J.-W.; Kim, M. K.; Cheng, H.; Yeo, W.-H.; Huang, X.; Liu, Y.; Zhang, Y.; Huang, Y.; Rogers, J. A. Capacitive Epidermal Electronics for Electrically Safe, Long-Term Electrophysiological Measurements. *Adv. Healthcare Mater.* **2014**, *3*, 642−648.
(48) Hwang, S.-W.; Lee, C. H.; Cheng, H.; Jeong, J.-W.; Kang, S.-K.; Kim, J.-H.; Shin, J.; Yang, J.; Liu, Z.; Ameer, G. A.; Huang, Y.; Rogers, J. A. Biodegradable Elastomers and Silicon Nanomembranes/Nanoribbons for Stretchable, Transient Electronics, and Biosensors. *Nano Lett.* **2015**, *15*, 2801−2808.
(49) Yamamoto, Y.; Yamamoto, D.; Takada, M.; Naito, H.; Arie, T.; Akita, S.; Takei, K. Efficient Skin Temperature Sensor and Stable Gel-Less Sticky Ecg Sensor for a Wearable Flexible Healthcare Patch. *Adv. Healthcare Mater.* **2017**, *6*, 1700495.
(50) Nemati, E.; Deen, M.; Mondal, T. A Wireless Wearable Ecg Sensor for Long-Term Applications. *IEEE Commun. Mag.* **2012**, *50*, 36−43.
(51) Meng, Y.; Li, Z.; Chen, J. A Flexible Dry Electrode Based on Aptes-Anchored Pdms Substrate for Portable Ecg Acquisition System. *Microsyst. Technol.* **2016**, *22*, 2027−2034.
(52) Yokus, M. A.; Jur, J. S. Fabric-Based Wearable Dry Electrodes for Body Surface Biopotential Recording. *IEEE Trans. Biomed. Eng.* **2016**, *63*, 423−430.
(53) Myers, A. C.; Huang, H.; Zhu, Y. Wearable Silver Nanowire Dry Electrodes for Electrophysiological Sensing. *RSC Adv.* **2015**, *5*, 11627−11632.
(54) Scalisi, R. G.; Paleari, M.; Favetto, A.; Stoppa, M.; Ariano, P.; Pandolfi, P.; Chiolerio, A. Inkjet Printed Flexible Electrodes for Surface Electromyography. *Org. Electron.* **2015**, *18*, 89−94.
(55) Mei, P.; Krusor, B.; Schwartz, D. E.; Ng, T. N.; Daniel, G.; Ready, S.; Whiting, G. L. Digital Fabrication and Integration of a Flexible Wireless Sensing Device. *IEEE Sens. J.* **2017**, *17*, 7114−7122.
(56) Mraović, M.; Muck, T.; Pivar, M.; Trontelj, J.; Pleteršek, A. Humidity Sensors Printed on Recycled Paper and Cardboard. *Sensors* **2014**, *14*, 13628−13643.
(57) Pichorim, S.; Gomes, N.; Batchelor, J. Two Solutions of Soil Moisture Sensing with Rfid for Landslide Monitoring. *Sensors* **2018**, *18*, 452.
(58) Lorenzen, J. A. Green Consumption and Social Change: Debates over Responsibility, Private Action, and Access. *Sociology Compass* **2014**, *8*, 1063−1081.
(59) Pramila, S.; Fulekar, M.; Bhawana, P. E-Waste-a Challenge for Tomorrow. *Res. J. Recent Sci.* **2012**, *1*, 86.
(60) Baker, M. I.; Walsh, S. P.; Schwartz, Z.; Boyan, B. D. A Review of Polyvinyl Alcohol and Its Uses in Cartilage and Orthopedic Applications. *J. Biomed. Mater. Res., Part B* **2012**, *100B*, 1451−1457.
(61) Mangels, A. R. Bone Nutrients for Vegetarians. *Am. J. Clin. Nutr.* **2014**, *100*, 469S−475S.
(62) Lara, H. H.; Ixtepan-Turrent, L.; Garza-Treviño, E. N.; Rodriguez-Padilla, C. PVP-coated silver nanoparticles block the transmission of cell-free and cell-associated HIV-1 in human cervical culture. *J. Nanobiotechnol.* **2010**, *8*, 15.
(63) Yong, X.; Schoonen, M. A. A. The Absolute Energy Positions of Conduction and Valence Bands of Selected Semiconducting Minerals. *Am. Mineral.* **2000**, *85*, 543−556.
(64) Wang, Y. U. Computer Modeling and Simulation of Solid-State Sintering: A Phase Field Approach. *Acta Mater.* **2006**, *54*, 953−961.
(65) Chockalingam, K.; Kouznetsova, V. G.; van der Sluis, O.; Geers, M. G. D. 2d Phase Field Modeling of Sintering of Silver Nanoparticles. *Comput. Methods Appl. Mech. Eng.* **2016**, *312*, 492.
(66) Kim, J.; Gutruf, P.; Chiarelli, A. M.; Heo, S. Y.; Cho, K.; Xie, Z.; Banks, A.; Han, S.; Jang, K.-I.; Lee, J. W.; Lee, K.-T.; Feng, X.; Huang, Y.; Fabiani, M.; Gratton, G.; Paik, U.; Rogers, J. A. Miniaturized Battery-Free Wireless Systems for Wearable Pulse Oximetry. *Adv. Funct. Mater.* **2017**, *27*, 1604373.

https://dx.doi.org/10.1021/acsami.0c11479
ACS Appl. Mater. Interfaces XXXX, XXX, XXX−XXX